

# Probing Cerium 4f States across the Volume Collapse Transition by X-ray Raman Scattering

Bijuan Chen,<sup>\*,†,∇</sup> Ekaterina M. Pärschke,<sup>\*,‡,∇</sup> Wei-Chih Chen,<sup>‡</sup> Brandon Scoggins,<sup>§</sup> Bing Li,<sup>†</sup> Mahalingam Balasubramanian,<sup>||</sup> Steve Heald,<sup>||</sup> Jianbo Zhang,<sup>†</sup> Hongshan Deng,<sup>†</sup> Raimundas Sereika,<sup>†</sup> Yesudhas Sorb,<sup>†</sup> Xia Yin,<sup>†</sup> Yan Bi,<sup>†</sup> Ke Jin,<sup>⊥</sup> Qiang Wu,<sup>⊥</sup> Cheng-Chien Chen,<sup>\*,‡,||</sup> Yang Ding,<sup>\*,†</sup> and Ho-kwang Mao<sup>†,#</sup>

<sup>†</sup>Center for High-Pressure Science & Technology Advanced Research, Beijing 100094, P.R. China

<sup>‡</sup>Department of Physics, University of Alabama at Birmingham, Birmingham, Alabama 35294, United States

<sup>§</sup>Department of Physics, University of North Georgia, Dahlonega, Georgia 30533, United States

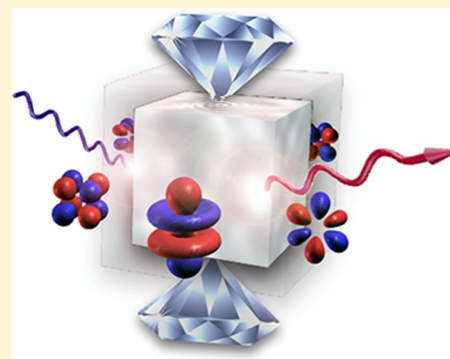
<sup>||</sup>Advanced Photon Source, Argonne National Laboratory, Argonne, Illinois 60439, United States

<sup>⊥</sup>National Key Laboratory of Shock Wave and Detonation Physics, Institute of Fluid Physics, CAEP, Mianyang 621900, China

<sup>#</sup>Geophysical Laboratory, Carnegie Institution of Washington, Washington, D.C. 20015, United States

## Supporting Information

**ABSTRACT:** Understanding the volume collapse phenomena in rare-earth materials remains an important challenge due to a lack of information on 4f electronic structures at different pressures. Here, we report the first high-pressure inelastic X-ray scattering measurement on elemental cerium (Ce) metal. By overcoming the ultralow signal issue in the X-ray measurement at the Ce  $N_{4,5}$ -edge, we observe the changes of unoccupied 4f states across the volume collapse transition around 0.8 GPa. To help resolve the longstanding debate on the Anderson–Kondo and Mott–Hubbard models, we further compare the experiments with extended multiplet calculations that treat both screening channels on equal footing. The results indicate that a modest change in the 4f–5d Kondo coupling can well describe the spectral redistribution across the volume collapse, whereas the hybridization between neighboring atoms in the Hubbard model appears to play a minor role. Our study helps to constrain the theoretical models and opens a promising new route for systematic investigation of volume collapse phenomena in rare-earth materials.



The unique electronic features of 4f electrons in rare-earth metals or the lanthanides have attracted much attention in recent years because of their wide ranges of potential applications.<sup>1,2</sup> Intriguingly, a number of lanthanide metals exhibit complex volume collapse transitions under high pressure, which is commonly associated with delocalization of the 4f electrons.<sup>3–5</sup> Pressure can enhance the screening of f electrons and effectively reduce electron correlation effects, eventually leading to a more itinerant and nonmagnetic state that favors a smaller volume. Theoretically, two scenarios for f electron delocalization under pressure have been proposed: the Mott–Hubbard model<sup>6</sup> and the Anderson–Kondo model.<sup>7,8</sup> The Mott–Hubbard model suggests that 4f electrons are more localized at individual Ce sites in the low-pressure  $\gamma$  phase, while in the high-pressure  $\alpha$  phase, they form delocalized bands due to enhanced hybridization between Ce atoms. Magnetic states emerge only in the low-pressure phase because of electron interaction effects. In the Anderson–Kondo model, the localized electrons are associated with 4f orbitals, and the itinerant electrons are related to conduction bands of mostly

6s5d character. In the low-pressure phase, the hybridization between localized and conduction states is small, rendering robust local moments and magnetic order. In the high-pressure phase, the local moments become screened by delocalized electrons, forming nonmagnetic Kondo singlets. Despite extensive studies, the microscopic origin of the screening mechanism remains a heated debate.<sup>6,7,9–12</sup>

In the past decade, synchrotron core-level spectroscopies have been employed widely to understand the properties of rare-earth metals under pressure. For instance, in 2006, Rueff et al. first applied  $L_{2,3}$ -edge (2p to 3d) resonant X-ray emission spectroscopy (RXES) to study cerium (Ce) metal.<sup>9</sup> The authors determined that the average 4f electron occupation changes from 0.97 to 0.81 across the volume collapse (at a transition pressure  $P_t \approx 0.8$  GPa at room temperature) and concluded that the transition is more consistent with the

Received: September 25, 2019

Accepted: November 14, 2019

Kondo model.<sup>9</sup> Using RXES, Maddox et al. in 2006 reached a similar conclusion for gadolinium (Gd).<sup>5</sup> In 2012, Lipp et al. applied  $L_{2,3}$ -edge nonresonant X-ray emission (NXES) to study Ce and reported a 30% decrease of its spin moment after the volume collapse. They also attributed the phase transition to the Kondo effect.<sup>13</sup> On the other hand, Bradley et al. in 2012 studied praseodymium (Pr) using RXES,<sup>14</sup> and their data can be explained by both the Kondo and Mott effects.<sup>14,15</sup> Fabbris et al. in 2013 applied X-ray absorption (XAS) and emission spectroscopy to study Gd and terbium (Tb). They proposed that in Tb, the volume collapse originates from the Kondo effect, whereas in Gd, it is of neither the Kondo nor Mott type.<sup>15,16</sup> More recently in 2019, Chiu et al. have applied NXES to study Ce and Pr, concluding that their volume collapse transitions both could be more closely related to Kondo effects.<sup>17</sup>

One major challenge in studying the volume collapse phenomena stems from a lack of information on the  $4f$  states at different pressures, as previous synchrotron spectroscopic experiments on rare-earth metals are essentially related to  $d$  states. Since there is only a small mixing of  $4f$  and  $d$  states, information about the electronic structure near the Fermi level (with mostly  $4f$  electrons) is limited. To overcome this challenge, here we apply for the first time high-pressure nonresonant inelastic X-ray scattering (NIXS) at the  $N_{4,5}$ -edge, which probes electron transition from the core  $4d$  levels to the unoccupied  $4f$  states near the Fermi level. Our spectroscopic measurements thereby provide invaluable information on the pressure evolution of  $4f$  electronic structures across the volume collapse transition.

Among the lanthanides, Ce has the simplest electronic configuration of one  $4f$  electron, and it also exhibits the largest pressure-induced volume reduction ( $\sim 15\%$ ) in the isostructural  $\gamma$  to  $\alpha$  phase transition at  $P_t \approx 0.8$  GPa at room temperature.<sup>18–20</sup> Ce has been extensively studied both experimentally and theoretically,<sup>21,22</sup> and the majority of the studies concluded that the itinerant behavior of  $4f$  electrons can be explained by increasing Kondo screening in the  $\alpha$  phase.<sup>9</sup> However, so far a definitive conclusion regarding the ultimate relevance of Kondo versus Mott–Hubbard models has not been reached.<sup>20,23</sup> By comparing the NIXS spectra of pure Ce metal with extended multiplet calculations, below we show that the spectral redistribution across the  $\gamma$  to  $\alpha$  transition can be accounted for by a modest change of  $\sim 0.5$  eV in the  $4f$ – $5d$  Kondo coupling, in agreement with our first-principles estimation.

Figure 1 shows a schematic diagram of the experimental setup and the geometry of the lower-energy-resolution inelastic X-ray scattering (LERIX) spectrometer. In high-pressure X-ray measurements, beryllium gaskets are usually used as X-ray windows. However, beryllium could not be adopted in our study, since its NIXS  $K$ -edge loss spectrum peaks in the energy range between 112 and 130 eV,<sup>24</sup> which overlaps with the Ce  $N_{4,5}$ -edge spectrum. Separating the signal of the sample from the gasket background can thereby become a serious problem (see Figure S1 in Supporting Information). To avoid this problem, we have developed a composite gasket made from a specially designed Kapton film and cubic boron nitride (c-BN), which allows the X-ray beam to enter and exit the sample chamber without causing a lot of background signal.

NIXS involving core-level states is typically referred to as X-ray Raman scattering (XRS). The cross section is proportional to the dynamic structure factor

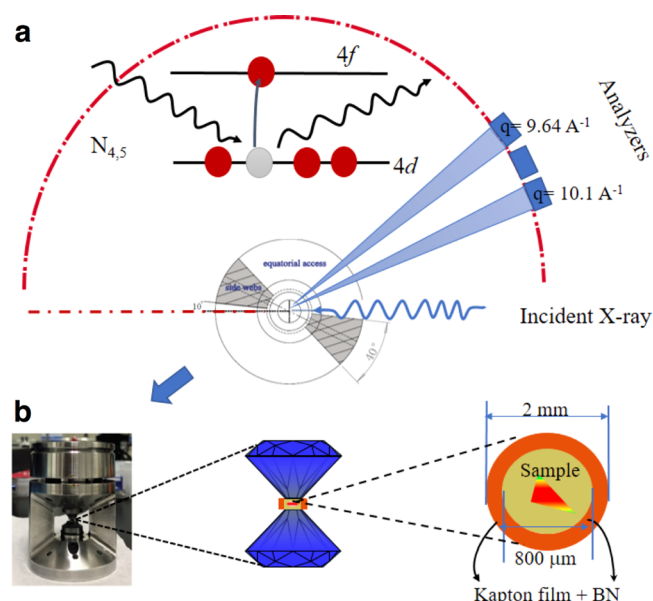


**Figure 1.** Schematic diagram of the inelastic X-ray scattering experimental setup. (a) Top view of the lower-energy-resolution inelastic X-ray scattering (LERIX) spectrometer for measuring the  $N_{4,5}$ -edge of Ce at high pressure, which probes the unoccupied  $f$  states near the Fermi level through  $4d$ – $4f$  excitations. Due to the strong background produced by the gasket below  $2\theta = 150^\circ$ , the signal only can be detected with analyzers placed at  $2\theta > 150^\circ$ . The incident X-ray beam is aligned approximately  $10^\circ$  to the axis of the side webs of the panoramic diamond anvil cell (DAC). (b) Side view showing the DAC. The Ce metal pellet is confined in a composite gasket made of c-BN powder and Kapton film. The incident X-ray energy is about 10 keV.

$$S(q, \omega) = \sum_f | \langle f | e^{iq \cdot r} | i \rangle |^2 \delta(E_f - E_i - \hbar\omega) \quad (1)$$

where  $i$  and  $f$  label respectively the initial and final states with corresponding energies  $E_i$  and  $E_f$ , and  $\hbar\omega$  is the photon energy transfer during the scattering process described by the momentum transfer  $q$ .<sup>25</sup> The scattering operator  $e^{iq \cdot r}$  can be expanded in terms of spherical harmonics,<sup>26–28</sup> and then, the total spectral intensity can be calculated as a sum of the individual isotropic  $k$ -pole spectra  $I^k(\omega)$  (see also [Experimental and Computational Methods](#)). The relative weight of each spectrum  $I^k(\omega)$  in the total sum depends strongly on the momentum transfer  $q$  and the rank of multipole  $k$ .<sup>28,29</sup> When  $q$  is sufficiently small, NIXS essentially measures the dipole ( $k = 1$ ) spectrum identical to XAS. In our experiments, however, the momentum transfer is between  $q \approx 9.64$ – $10 \text{ \AA}^{-1}$ , so the spectra are mainly governed by octupole ( $k = 3$ ) and triakontadipole ( $k = 5$ ) transitions, with a ratio  $R \approx 7$ – $8$  between the  $k = 3$  and  $k = 5$  branches.<sup>27</sup> The ground state of a  $4f^1$  shell has orbital angular momentum  $L = 3$ , so the maximal allowed final states  $L$  are 6 and 8, respectively, with  $k = 3$  and 5 multipole transitions. The average peak energy will shift toward lower energy with increasing  $L$ .

Figure 2 shows the  $q$ -dependent XRS spectra collected respectively in the  $\gamma$  phase at 0.48 GPa (below  $P_t$ ) and the  $\alpha$  phase at 1.97 GPa (above  $P_t$ ). The prethreshold region ranging from 101 to 115 eV is related to excitations of core-level  $4d$  electrons onto unoccupied  $4f$  multiplet states. As the system transits from the  $\gamma$  phase to the  $\alpha$  phase, the width of the prepeak around 106 eV narrows, and its intensity reduces by  $\sim 27\%$ . The prepeak position also shifts by  $\sim 0.4$  eV to lower

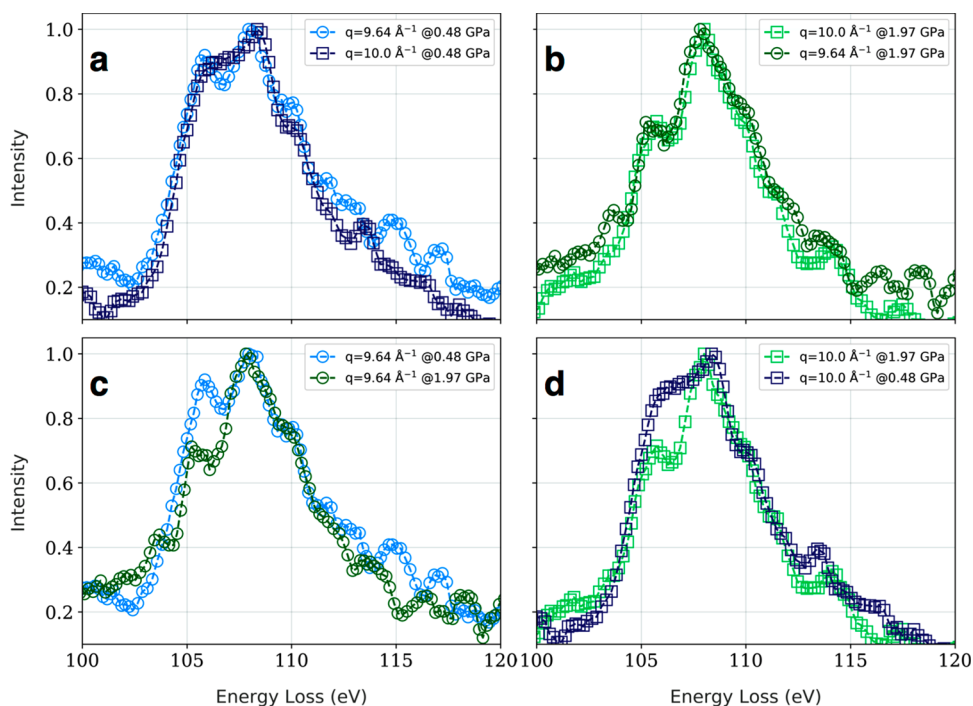


**Figure 2.** Experimental nonresonant inelastic X-ray scattering (NIXS) spectra at Ce  $N_{4,5}$ -edge across the transition pressure  $P_t$  for volume collapse transition. (a) Momentum-transfer  $q$ -dependence of NIXS spectra at 0.48 GPa ( $\gamma$  phase). (b) Momentum transfer  $q$ -dependence of NIXS spectra at 1.97 GPa ( $\alpha$  phase). (c) Comparison of NIXS spectra at 0.48 GPa (blue line, below  $P_t$ ) and 1.97 GPa (green line, above  $P_t$ ) at  $q = 9.64 \text{ \AA}^{-1}$ . (d) Comparison of NIXS spectra at 0.48 GPa (blue line, below  $P_t$ ) and 1.97 GPa (green line, above  $P_t$ ) at  $q = 10.0 \text{ \AA}^{-1}$ . The most prominent difference between low- and high-pressure spectra lies in the change of peak intensity at  $\sim 106 \text{ eV}$ . The spectral intensity as calculated using the sum rule in refs 54 and 55 is normalized to the main peak, and the signals due to valence-electron Compton scattering were removed.

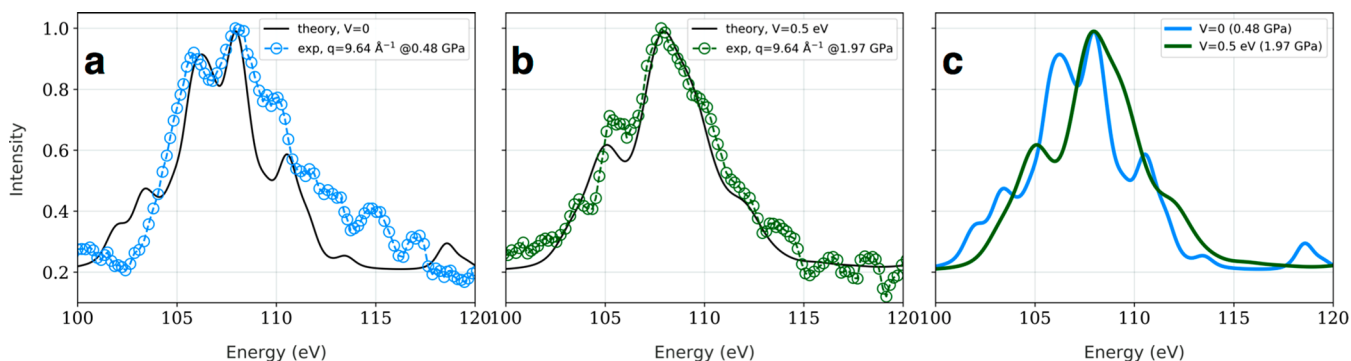


**Figure 3.** Comparisons between extended atomic multiplet calculations to Ce  $N_{4,5}$ -edge NIXS spectra. The theory spectrum is a sum of octupole ( $k = 3$ ) and triakontadipole ( $k = 5$ ) transitions, with an intensity ratio of  $R \approx 8$ . (a) The  $V = 0$  calculation (black curve) reproduces the main features of the low-pressure 0.48 GPa experiment at momentum transfer  $q = 9.64 \text{ \AA}^{-1}$  (blue line). (b) The calculation with an effective Kondo coupling of  $V = 0.5 \text{ eV}$  (black curve) matches our NIXS experiment well at pressure of 1.97 GPa and  $q = 9.64 \text{ \AA}^{-1}$  (green line). (c) Comparison of theory spectra with different strengths of  $V$ . The drop in peak intensity at  $\sim 106 \text{ eV}$  with increasing Kondo coupling is consistent with the experiments across the volume collapse transition.

energy. Due to the strong Compton scattering occurring at a smaller angle  $\theta$  between the gasket and diamond anvil cell (DAC), the signal from the sample only can be collected with four of the analyzers situated at  $2\theta > 150^\circ$ , which corresponds to momentum transfers  $q = 9.64$  to  $10 \text{ \AA}^{-1}$  in a vertical scattering plane. In this  $q$  range, the Compton scattering from gasket ceases, and the excitation processes in Ce are dominated by high-order multipole transitions as described before.<sup>25,29–31</sup> In contrast to the broad XAS spectra with a dipole transition, the sharper spectral features with higher-multipole transitions involving larger angular momentum transfer in XRS will enable

more detailed comparison between experiment and model simulation of Ce's electronic structure.

At ambient pressure, the Ce NIXS spectra are well described by atomic multiplet calculations<sup>32,33</sup> extended to higher-rank multiplet transitions.<sup>26,30,31,34</sup> To model the changes in the spectra occurring after the volume collapse, we extend the atomic multiplet calculations by including both Kondo and Mott screening effects. In addition to the on-site  $4f$  and  $4d$  spin-orbit couplings as well as  $4f-4f$  and  $4f-4d$  electron-electron interactions, our model includes Kondo coupling  $V$  between  $4f$  electrons and the conduction bands (with mostly unfilled  $5d$  orbitals). It also contains the direct hybridization between  $f$

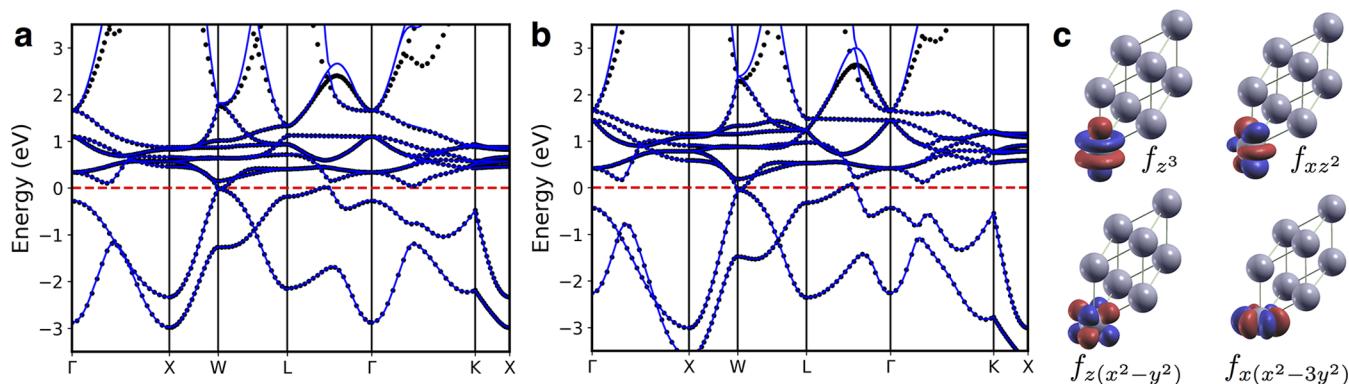


**Figure 4.** Electronic structure and Wannier-orbital calculations based on density functional theory (DFT). (a) DFT (black dots) and Wannier (blue curves) band structure calculations for FCC cerium at ambient pressure. Excellent agreements between DFT and Wannier calculations are obtained between  $-3$  to  $2$  eV around the Fermi level (indicated by the horizontal dashed red line). (b) DFT (black dots) and Wannier (blue curves) band structure calculations for high-pressure FCC cerium with  $\sim 15\%$  volume reduction. The pressure-induced band broadening effect is more apparent for the  $s$  or  $d$  bands, while for  $f$  orbitals (in the energy range of  $\sim -1$  to  $1$  eV), the effect is much weaker. (c) Schematic cartoons showing the maximally localized Wannier functions of selected  $4f$  orbitals.

orbitals on neighboring Ce atoms in a Mott–Hubbard model. The  $f$ – $f$  hopping elements are calculated using Slater–Koster tables and depend on four two-center integrals  $V_\sigma$ ,  $V_\pi$ ,  $V_\delta$ , and  $V_\varphi$ ,<sup>35</sup> which are parametrized as  $V_\sigma = t$ ,  $V_\pi = -0.75t$ ,  $V_\delta = 0.3t$ , and  $V_\varphi = -0.05t$ .<sup>36</sup> When the Kondo coupling  $V$  and  $f$ – $f$  hopping  $t$  are both set to zero, our model reduces to a pure atomic multiplet calculation,<sup>37</sup> which has been utilized to model earlier ambient-pressure NIXS data.<sup>26</sup> Below, we vary the strengths of Kondo coupling  $V$  and  $f$ – $f$  hopping  $t$  in the model Hamiltonian to simulate how different screening channels affect the NIXS spectra at high pressure. We will focus on the pressure evolution of spectral trends and discuss the results at a semiquantitative level.

Figure 3 compares the theory spectra and experiments at momentum transfer  $q = 9.64 \text{ \AA}^{-1}$ . The  $V = 0$  calculation (black curve) in Figure 3a shows the main experimental features at  $0.48$  GPa (blue line), with a two-peak structure at  $106$  and  $108$  eV. The higher-energy shoulder peak at  $\sim 110$  eV is underestimated, potentially due to a band broadening effect that is not captured by our finite-size cluster calculation. With increasing Kondo coupling  $V$ , the peak intensity at  $\sim 106$  eV drops accordingly. The best fit to the high-pressure experiment at  $1.97$  GPa is shown in Figure 3b; the calculation employs an effective Kondo coupling  $V = 0.5$  eV and  $f$ – $f$  hopping  $t = 0$ . The high-pressure experimental features (green line) are reproduced by our model calculations with reasonably good agreement. Some theory–experiment mismatch can be attributed additionally to the deviation in the experimental spectra upon small changes of momentum  $q$  (see Figure 2b). Moreover, it has been shown previously<sup>12,38,39</sup> that while the ratio between singly and doubly occupied  $f$  orbitals of the ground state in the  $\gamma$  phase is  $n(f^1)/n(f^2) \approx 20$ , this ratio is likely to decrease in the  $\alpha$  phase, resulting in a small but noticeable contribution from the  $f^2$  component. Previous experiments and theory have indicated different degrees of  $f^2$  admixture to the ground state in the  $\alpha$  phase,<sup>12,38,39</sup> which are not accounted for in our calculation.

To further estimate the change in the Kondo coupling across the volume collapse, we perform density functional theory (DFT) and Wannier-orbital calculations to extract the hybridization parameters (see Figure 4). After the volume collapse, the Wannierization results suggest a change of  $4f$ – $5d$  hybridization  $V = 0.516$  eV, which is very close to our choice of

$V = 0.5$  eV for the high-pressure experiments. Moreover, a Kondo coupling  $V = 0.5$  eV in our extended multiplet model will produce an average  $4f$  electron occupation  $\langle n_f \rangle \approx 0.83$  (see Figure S2), which also agrees well with previous estimation of  $\langle n_f \rangle \approx 0.8$  after the volume collapse transition.<sup>9,13,39</sup> While pure DFT may be more limited in certain aspects,<sup>40,41</sup> advanced ab initio dynamical mean-field theory (DFT + DMFT) studies<sup>42–44</sup> have suggested that the Kondo mechanism can describe optical and photoemission experiments better than a Mott picture. Our combined theoretical and experimental NIXS studies that probe unoccupied Ce  $4f$  orbitals appear to point to the same conclusion.

We next test if direct  $f$ – $f$  hybridization between neighboring atoms as in a Mott–Hubbard model could in principle account for the high-pressure spectra (see Supporting Information for additional simulated spectra). We find that to achieve a significant effect on the spectra with  $f$ – $f$  hopping, an unrealistically large value of  $t \approx 2$  eV is needed, which is particularly unreasonable considering that  $f$  orbitals are spatially much more confined than  $s$ ,  $p$ , or  $d$  orbitals. In our DFT Wannier-orbital calculation, the largest hopping element between neighboring  $f$  orbitals is  $\tau(z^2, z^2)$ , which changes from  $0.108$  eV at ambient conditions to  $0.148$  eV under high pressure. It describes the overlap between  $z(5z^2-3r^2)$  orbitals along the  $z$ -axis. Using  $\tau(z^2, z^2) = 5/8V_{ff\pi} + 5/8V_{ff\varphi}$ ,<sup>35</sup> we estimate that  $t = 0.473$  eV under high pressure, which is much smaller than the required  $t \approx 2$  eV to fit the experiment. Even if one assumes an unrealistically large  $f$ – $f$  hopping amplitude, the agreement between theory and experiment is in general poorer than that in the Kondo calculation (see Figure S3). In addition, a very large  $t$  alone would result in an average  $4f$  occupation  $\langle n_f \rangle \approx 1$ , which contradicts with previous high-pressure experimental findings. In general, with  $V \approx 0.5$ – $0.55$  eV, we do not find any further improvement in fitting the spectra by tuning  $t$  (see Figure S4).

We also have considered other effects that might change the high-pressure spectra. First, we have studied ligand crystal-field effects by adding finite energy splitting in the  $f$  orbitals, but we have not found any apparent improvement on the theory–experiment agreement within a reasonable range of parameters. This is consistent with our DFT calculations showing that the  $f$  orbital energy-level splitting increases only by  $\sim 0.05$  eV under pressure. Second, we have considered the effect of a finite  $5d$

bandwidth up to 3 eV but again have not observed any appreciable change in the multiplet spectra. The pressure-induced  $5d$  band broadening is at most 0.5 eV in our DFT calculations. We also note that since our model explicitly contains multiplet interactions, these effects should not be included in DFT calculations to avoid double counting.

Finally, it is worth noting that the resulting NIXS spectra are dependent on the intensity ratio  $R$  between the octupole ( $k = 3$ ) and triakontadipole ( $k = 5$ ) transitions.  $R$  scales as a square of the ratio between the expectation values of radial  $k = 3$  and  $k = 5$  wave functions, and  $R$  is equal to  $\sim 7$  based on Hartree–Fock calculations.<sup>27</sup> Since Hartree–Fock approximation is known to underestimate the extent of radial wave functions by at least 15%, here we adopt the value of  $R = 8$  instead of 7 as directly from ref 27. The agreement between theory and experiment is similar for either  $R$  value. While in principle  $R$  could further depend on pressure, our Wannier-orbital calculations show that the radial spread of  $4f$  wave functions changes at most by 0.5% under compression. Therefore, a pressure-independent  $R$  as employed in our study is a valid assumption.

In conclusion, the development of multielement XRS spectrometers has allowed, for the first time, the probing of  $4f$  states in cerium under high pressure across the volume collapse transition. A detailed experiment–theory comparison suggests that cerium’s  $N_{4,5}$ -edge spectral redistribution across the isostructural transition from the  $\gamma$  to  $\alpha$  phases can be reasonably accounted for by the Kondo mechanism, while the role of Mott–Hubbard transition appears to be more minor. However, a nonzero, albeit small,  $f$ – $f$  hybridization coexisting with Kondo coupling may account for the transition line in the experimental pressure–temperature phase diagram.<sup>33</sup> These results have successfully benchmarked previous theories and helped to pin down cerium’s volume collapse mechanism. Our work also opens up new opportunities for studying a wide range of pressure-induced phenomena, including volume collapse, valence transition, and quantum critical fluctuations.<sup>3,37</sup> Similar experiments and calculations for other rare-earth materials showing volume collapse transitions will be interesting areas of future studies.

## EXPERIMENTAL AND COMPUTATIONAL METHODS

**Sample preparation.** The sample assembly is very important to this experiment. Maximum care was taken to avoid any cerium oxidation during the loading and measurement stages (see also Figure S5 in the Supporting Information). High-purity polycrystalline Ce foils with 25  $\mu\text{m}$  thickness were purchased from Goodfellow with at least 99.9% purity. The impurities level of our sample compares well with other previous XRS experiments that used Ce foils.<sup>26</sup> A small chip of Ce was cut off directly from the Ce foils in silicone oil<sup>9</sup> and loaded in a panoramic type diamond anvil cell (DAC). A pair of type Ia diamond anvils from Almax easyLab with an 800  $\mu\text{m}$  culet diameter was used for experiments. The entire loading process was conducted inside an argon-filled glovebox with high-purity Ar atmosphere ( $\text{O}_2 < 0.1$  ppm,  $\text{H}_2\text{O} < 0.01$  ppm) within several minutes. A modified gasket made of Kapton polyimide film combined with the cubic boron nitride (c-BN) was used to maximize the X-ray access geometry and minimize the background from the gasket. The panoramic DAC has two 40° symmetrical side windows with 140° equatorial access to allow easy side X-ray beam transmission. The 700  $\mu\text{m}$  thick Kapton

polyimide film gasket has a shape of a concentric disc of 2 mm in diameter. The disc has a hole of 800  $\mu\text{m}$  in diameter filled with a 70  $\mu\text{m}$  thick layer of c-BN. A hole with the diameter of 60  $\mu\text{m}$  was drilled at the center of the c-BN gasket to form the sample chamber. The 20  $\mu\text{m}$  thick sample was cut into a  $30 \times 40 \times 50 \mu\text{m}^3$  triangle to maximize the backscattering signals, as shown in Figure 1. Several pieces of fine-grained ruby were placed on the sides of the sample as the pressure markers.<sup>3,45</sup> The sample chamber was sealed at  $\sim 0.48$  GPa with silicone oil as the pressure medium.

**Nonresonant inelastic X-ray scattering measurements.** The momentum transfer  $q$ -dependent nonresonant inelastic X-ray scattering (NIXS) measurements were performed with the lower-energy-resolution inelastic X-ray scattering (LERIX)<sup>29</sup> spectrometer at the X-ray Science Division (XSD) beamline 20-ID of the Advance Photon Source, Argonne National Laboratory, using a double-bounce Si(111) monochromator with the resolution of 1.3 eV. The DAC was mounted on the rotation axis of the inner part of the LERIX spectrometer and oriented so that the X-rays were incident approximately 10° to the axis of the side webs of DAC (Figure 1). The monochromatic incident X-ray beam was focused to a  $10 \times 15 \mu\text{m}$  ( $H \times V$ ) spot and passed through the gasket in the gap between the diamond anvils in the radial orientation. The scattering NIXS signals were collected with dispersions in the vertical plane. Spectrometer performance and operation were in accord with previous work.<sup>2,3,34,46</sup> In the present experiments, the LERIX instrument provided simultaneous measurement of  $S(q, \omega)$  at momentum transfers  $q \approx 9.64$ – $10.0 \text{ \AA}^{-1}$  by configuring a four-detector (spherically bent Si(555), from the 16th to 19th detector) array measuring. Low-momentum-transfer data from the sample were covered by the strong background signals from gasket and DAC. The experimental data were collected on a so-called inverse scanning mode, where the analyzer crystals were kept fixed, and the incident beam energy was scanned from 90 to 130 eV above the elastic scattering energy of 9890 eV. During measurements, samples were always held in a flowing helium environment.

**Extended atomic multiplet calculations.** The full Hamiltonian describing the system is

$$H = H_{\text{multiplet}} + H_{\tau} + H_{\text{Kondo}} \quad (2)$$

Besides  $4d$  ( $4f$ ) on-site spin–orbit coupling  $\lambda_{4d} = 1.2$  eV ( $\lambda_{4f} = 0.1$  eV), the multiplet Hamiltonian  $H_{\text{multiplet}}$  includes  $4f$ – $4f$  electron–electron and  $4f$ – $4d$  electron–hole interactions as well as the on-site energy  $\epsilon_r$  for  $4d$  orbitals, chosen to match the white line of the Ce  $N_{4,5}$ -absorption edge:

$$\begin{aligned} H_{\text{multiplet}} = & \sum_{r \in 4d} \lambda_{4d} l_r \cdot s_r + \sum_{r \in 4f} \lambda_{4f} l_r \cdot s_r \\ & + \sum_{i\alpha\alpha' \beta\beta' \sigma\sigma'} (U_{\alpha\alpha' \beta\beta'}^{ff} f_{i\alpha\sigma}^{\dagger} f_{i\alpha'\sigma'} f_{i\beta\sigma} f_{i\beta'\sigma'}^{\dagger}) \\ & + U_{\alpha\alpha' \beta\beta'}^{df, \text{direct}} d_{i\alpha\sigma}^{\dagger} f_{i\alpha'\sigma'} f_{i\beta\sigma}^{\dagger} d_{i\beta'\sigma} \\ & + U_{\alpha\alpha' \beta\beta'}^{df, \text{exchange}} f_{i\alpha\sigma}^{\dagger} d_{i\beta\sigma} f_{i\alpha'\sigma'}^{\dagger} d_{i\beta'\sigma} \end{aligned} \quad (3)$$

The hopping part of the Mott–Hubbard Hamiltonian is written as

$$H_{\tau} = - \sum_{(i,j)\alpha\beta\sigma} \tau_{\alpha\beta} f_{i\alpha\sigma}^{\dagger} f_{j\beta\sigma} + H.c. \quad (4)$$

and the Kondo Hamiltonian is

$$H_{Kondo} = V \sum_{i\alpha\sigma} (c_{i\alpha\sigma}^\dagger + H. c.) + \sum_{k\sigma} \epsilon_k c_{k\sigma}^\dagger c_{k\sigma} \quad (5)$$

Here, the  $c_{i\alpha\sigma}^\dagger (f_{i\alpha\sigma}^\dagger d_{i\alpha\sigma}^\dagger)$  operator creates an electron in the  $5d$  conduction band (on  $4f$ ,  $4d$  orbital  $\alpha$ ) on site  $i$  with spin projection  $s_z = \sigma$ . Because of the large  $d$ - $d$  hybridization between neighboring atoms ( $t_{dd} = 1.9$  eV under high pressure as estimated in our DFT calculations), we consider  $5d$  orbitals as a conduction band rather than distinguishable localized atomic orbitals. In our calculations, we have included five effective conduction bands and two cerium atoms. Besides  $4f$ - $4f$  electron-electron interactions, the Hamiltonian (eq 2) contains  $4d$ - $4f$  core-hole interactions to account for the  $4d^2 4f^2$  excited state configurations in the  $N_{4,5}$ -edge spectroscopy. These interactions are described by orbital-dependent Coulomb repulsion matrices  $U_{\alpha\alpha'\beta\beta'}^{ff}$ ,  $U_{\alpha\alpha'\beta\beta'}^{df, direct}$ , and  $U_{\alpha\alpha'\beta\beta'}^{df, exchange}$ ,<sup>47</sup> which depend on the following Slater-Condon parameters:<sup>47</sup>  $F_{ff}^0 = 5$  eV,  $F_{ff}^2 = 10.1$  eV,  $F_{ff}^4 = 6.35$  eV,  $F_{ff}^6 = 4.57$  eV,  $F_{df}^0 = 5$  eV,  $F_{df}^2 = 10.3$  eV,  $F_{df}^4 = 6.6$  eV,  $G_{df}^1 = 10.13$  eV,  $G_{df}^3 = 6.36$  eV, and  $G_{df}^5 = 4.49$  eV. The hopping elements  $\tau_{\alpha\beta\sigma}$  were calculated using Slater-Koster tables for  $f$  electrons, and they depend on four two-center integrals  $V_{\sigma\sigma}$ ,  $V_{\pi\pi}$ ,  $V_{\delta\delta}$ , and  $V_{\varphi\varphi}$ <sup>35</sup> which are parametrized as  $V_{\sigma\sigma} = t$ ,  $V_{\pi\pi} = -0.75t$ ,  $V_{\delta\delta} = 0.3t$ , and  $V_{\varphi\varphi} = -0.05t$ .<sup>36</sup> The center of gravity for the  $5d$  conduction band energy  $\epsilon_r$  is chosen to account for the energy shift introduced by  $F_0$ .

The nonresonant X-ray scattering cross section is proportional to the dynamic structure factor

$$S(q, \omega) = \sum_f | \langle f | e^{iq \cdot r} | i \rangle |^2 \delta(E_f - E_i - \hbar\omega) \quad (6)$$

where  $|i\rangle(|f\rangle)$  is the initial (final) state with energy  $E_i$  ( $E_f$ ), obtained by exact diagonalization of the model.  $\hbar\omega$  is the energy loss of the incident photon, and  $q$  is the corresponding momentum transfer. One can expand the transition operator  $e^{iq \cdot r}$  in eq 6 in terms of spherical harmonics<sup>27,28</sup>

$$e^{iq \cdot r} = \sum_{k=0}^{\infty} \sum_{m=-k}^k i^k (2k+1) j_k(qr) C_m^{(k)*}(\theta_q, \varphi_q) C_m^{(k)}(\theta_r, \varphi_r) \quad (7)$$

where  $j_k(qr)$  represents spherical Bessel functions of rank  $k$ ,  $C_m^{(k)} = \sqrt{\frac{4\pi}{2k+1}} Y_{km}$ , and  $Y_{km}$  represents the spherical harmonics.

The radial matrix element that arises from substituting eq 7 into eq 6 depends strongly on  $q$  but varies slowly over the energy scale of the spectrum. Therefore, it can be factored out of the sum over the final states in eq 6, and the total intensity can be calculated as a sum of individual isotropic  $k$ -pole spectra  $I^k(\omega)$  written as

$$I^k(\omega) = \sum_f \sum_{m=-k}^k | \langle f | C_m^{(k)} | i \rangle |^2 \delta(E_f - E_i - \hbar\omega) \quad (8)$$

The relative weight of  $I^k(\omega)$  in the total sum depends strongly on the momentum transfer  $q$  and the multipole rank  $k$ ,<sup>28</sup> since the expectation value of a spherical Bessel function depends on  $q$ .<sup>27</sup> For  $N_{4,5}$ -edge NIXS involving  $4d$ - $4f$  excitations, the allowed transitions are monopole ( $k = 1$ ), octupole ( $k = 3$ ), and triakontadipole ( $k = 5$ ) terms, due to selection rule and angular momentum conservation. The final simulated spectra were convolved with a Lorentzian of half-width  $\Gamma = 0.15$  eV to account for intrinsic line width and a Gaussian of  $\sigma = 0.3$  (0.5) eV at low (high) pressure to mimic finite experimental resolution and additional broadening introduced by bulk as compared to a small cluster calculation.

**Density functional theory and Wannier-orbital calculations.** To study the orbital spreads, we utilize Wannier90 package<sup>48</sup> to construct maximally localized Wannier functions (MLWFs) from eigenfunctions of fully relaxed face-centered cubic (FCC) Ce as well as a high-pressure unit cell with  $\sim 15\%$  volume reduction compared to the ambient structure. The eigenfunctions are obtained by density functional theory (DFT) using the VASP (Vienna Ab initio Simulation Package) package,<sup>49,50</sup> which adopts the plane wave pseudopotential approach. In our DFT calculations, the projector augmented wave method<sup>51,52</sup> with the PBE/GGA exchange correlation functional<sup>53</sup> is used. The plane wave cutoff energy is set to be 600 eV, and the  $\Gamma$ -centered  $15 \times 15 \times 15$   $k$ -point sampling in the Brillouin zone is considered. The ambient structure is relaxed until the force on Ce is less than  $10^{-3}$  eV/Å, and an energy difference of less than  $10^{-6}$  eV/unit cell was set for the electronic loop convergence criterion. To obtain 13 MLWFs, 44 bands are included for the disentanglement procedure in the calculations. The maxima of the outer and lower windows are set to 64.4 and 2 eV, respectively. The 13 MLWFs are constructed using one  $s$ , seven  $f$ , and five  $d$  orbitals as the initial trial localized orbitals, and the final spreads (less than 2.85 Å) are checked carefully. These MLWFs are then used to reconstruct the 13 bands near the Fermi level (see Figure 4).

## ■ ASSOCIATED CONTENT

### Supporting Information

The Supporting Information is available free of charge at <https://pubs.acs.org/doi/10.1021/acs.jpcclett.9b02819>.

Experimental X-ray spectra collected using different gaskets, X-ray diffraction patterns of different cerium systems, and additional simulated X-ray spectra for the Kondo and Hubbard models (PDF)

## ■ AUTHOR INFORMATION

### Corresponding Authors

\*E-mail: [bijuan.chen@hpstar.ac.cn](mailto:bijuan.chen@hpstar.ac.cn). (B.C.)

\*E-mail: [katjap@uab.edu](mailto:katjap@uab.edu). (E.M.P.)

\*E-mail: [chenc@uab.edu](mailto:chenc@uab.edu). (C.-C.C.)

\*E-mail: [yang.ding@hpstar.ac.cn](mailto:yang.ding@hpstar.ac.cn). (Y.D.)

### ORCID

Steve Heald: 0000-0002-4369-8248

Jianbo Zhang: 0000-0002-8339-1099

Raimundas Sereika: 0000-0001-5365-6773

Cheng-Chien Chen: 0000-0001-9931-615X

### Author Contributions

<sup>‡</sup>B.C. and E.M.P. contributed equally to this work.

### Notes

The authors declare no competing financial interest.

## ■ ACKNOWLEDGMENTS

The authors thank Maurits Haverkort for helpful discussion on the atomic multiplet calculations. Y.D. acknowledges support from the Science Challenge Project No. TZ2016001 and NSAF grant No. U1930401. The inelastic X-ray scattering experiments were performed at beamline 20-ID and the X-ray diffraction measurements were performed at sector 16 BM-D of the Advanced Photon Source, a U.S. Department of Energy (DOE) Office of Science user facility operated by Argonne National Laboratory (ANL) supported by the U.S. DOE Award No. DE-AC02-06CH11357. Y.D. and B.C. acknowledge

support on the XRD experiments from beamline scientist Curtiss Kenney-Benson at sector 16 BM-D of the Advanced Photon Source. Y.D. and H.-k.M. acknowledge support from DOE-BES under Award No. DE-FG02-99ER45775 and NSF Grant No. U1530402. B.S. acknowledges support from the UAB NSF REU program under award No. DMR-1754078. This work is also supported by National Natural Science Foundation of China (NSFC) No. 11874075 and National Key R&D Program of China No. 2018YFA0305703.

## REFERENCES

- (1) Gutfleisch, O.; Willard, M. A.; Bruck, E.; Chen, C. H.; Sankar, S. G.; Liu, J. P. Magnetic Materials and Devices for the 21st Century: Stronger, Lighter, and More Energy Efficient. *Adv. Mater.* **2011**, *23*, 821–842.
- (2) Pfleiderer, C. Superconducting Phases of *f*-Electron Compounds. *Rev. Mod. Phys.* **2009**, *81*, 1551–1624.
- (3) Mao, H. K.; Chen, X. J.; Ding, Y.; Li, B.; Wang, L. Solids, Liquids, and Gases under High Pressure. *Rev. Mod. Phys.* **2018**, *90*, No. 015007.
- (4) Olijnyk, H.; Grosshans, W. A.; Jephcoat, A. P. Lattice Vibrations and Electronic Transitions in the Rare-Earth Metals: Praseodymium under Pressure. *Phys. Rev. Lett.* **2004**, *93*, 255505.
- (5) Maddox, B. R.; Lazicki, A.; Yoo, C. S.; Iota, V.; Chen, M.; McMahan, A. K.; Hu, M. Y.; Chow, P.; Scalettar, R. T.; Pickett, W. E. 4*f* Delocalization in Gd: Inelastic X-Ray Scattering at Ultrahigh Pressure. *Phys. Rev. Lett.* **2006**, *96*, 215701.
- (6) Johansson, B. The  $\alpha$ - $\gamma$  Transition in Cerium is a Mott Transition. *Philos. Mag.* **1974**, *30*, 469–482.
- (7) Allen, J. W.; Martin, R. M. Kondo Volume Collapse and the  $\gamma \rightarrow \alpha$  Transition in Cerium. *Phys. Rev. Lett.* **1982**, *49*, 1106–1110.
- (8) Lavagna, M.; Lacroix, C.; Cyrot, M. Volume Collapse in the Kondo Lattice. *Phys. Lett. A* **1982**, *90*, 210–212.
- (9) Rueff, J. P.; Itie, J. P.; Taguchi, M.; Hague, C. F.; Mariot, J. M.; Delaunay, R.; Kappler, J. P.; Jaouen, N. Probing the Transition in Bulk Ce under Pressure: A Direct Investigation by Resonant Inelastic X-Ray Scattering. *Phys. Rev. Lett.* **2006**, *96*, 237403.
- (10) Lipp, M. J.; Jenei, Z.; Cynn, H.; Kono, Y.; Park, C.; Kenney-Benson, C.; Evans, W. J. Anomalous Elastic Properties across the  $\gamma$  to  $\alpha$  Volume Collapse in Cerium. *Nat. Commun.* **2017**, *8*, 1198.
- (11) Bustingorry, S.; Jagla, E. A.; Lorenzana, J. Thermodynamics of Volume-Collapse Transitions in Cerium and Related Compounds. *Acta Mater.* **2005**, *53*, 5183–5188.
- (12) Rueff, J.-P.; Hague, C. F.; Mariot, J.-M.; Journal, L.; Delaunay, R.; Kappler, J.-P.; Schmerber, G.; Derory, A.; Jaouen, N.; Krill, G. *f*-State Occupancy at the  $\gamma$ - $\alpha$  Phase Transition of Ce-Th and Ce-Sc Alloys. *Phys. Rev. Lett.* **2004**, *93*, No. 067402.
- (13) Lipp, M. J.; Sorini, A. P.; Bradley, J.; Maddox, B.; Moore, K. T.; Cynn, H.; Devereaux, T. P.; Xiao, Y.; Chow, P.; Evans, W. J. X-Ray Emission Spectroscopy of Cerium across the  $\gamma$ - $\alpha$  Volume Collapse Transition. *Phys. Rev. Lett.* **2012**, *109*, 195705.
- (14) Bradley, J. A.; Moore, K. T.; Lipp, M. J.; Mattern, B. A.; Pacold, J. I.; Seidler, G. T.; Chow, P.; Rod, E.; Xiao, Y. M.; Evans, W. J. 4*f* Electron Delocalization and Volume Collapse in Praseodymium Metal. *Phys. Rev. B: Condens. Matter Mater. Phys.* **2012**, *85*, 100102R.
- (15) McMahan, A. K.; Scalettar, R. T.; Jarrell, M. Screening of 4*f* Moments and Delocalization in the Compressed Light Rare Earths. *Phys. Rev. B: Condens. Matter Mater. Phys.* **2009**, *80*, 235105.
- (16) Fabbris, G.; Matsuoka, T.; Lim, J.; Mardegan, J. R. L.; Shimizu, K.; Haskel, D.; Schilling, J. S. Different Routes to Pressure-Induced Volume Collapse Transitions in Gadolinium and Terbium Metals. *Phys. Rev. B: Condens. Matter Mater. Phys.* **2013**, *88*, 245103.
- (17) Chiu, W. T.; Mortensen, D. R.; Lipp, M. J.; Resta, G.; Jia, C. J.; Moritz, B.; Devereaux, T. P.; Savrasov, S. Y.; Seidler, G. T.; Scalettar, R. T. Pressure Effects on the 4*f* Electronic Structure of Light Lanthanides. *Phys. Rev. Lett.* **2019**, *122*, No. 066401.
- (18) Koskenmaki, D. C.; Gschneidner, Jr., K. A. Chapter 4 Cerium. *Handbook on the Physics and Chemistry of Rare Earths*; Gschneidner, Jr., K. A., Eyring, L., Eds.; Elsevier, 1978; Vol. 1, pp 337–377.
- (19) McMahan, A. K.; Huscroft, C.; Scalettar, R. T.; Pollock, E. L. Volume-Collapse Transitions in the Rare Earth Metals. *J. Comput.-Aided Mater. Des.* **1998**, *5*, 131–162.
- (20) Johansson, B.; Ruban, A. V.; Abrikosov, I. A. Comment on “Thermal Signatures of the Kondo Volume Collapse in Cerium”. *Phys. Rev. Lett.* **2009**, *102*, 189601.
- (21) Nikolaev, A. V.; Tsvyashchenko, A. V. The Puzzle of the  $\gamma \rightarrow \alpha$  and other Phase Transitions in Cerium. *Phys.-Usp.* **2012**, *55*, 657–680.
- (22) Weschke, E.; Laubschat, C.; Simmons, T.; Domke, M.; Strebler, O.; Kaindl, G. Surface and Bulk Electronic Structure of Ce Metal Studied by High-Resolution Resonant Photoemission. *Phys. Rev. B: Condens. Matter Mater. Phys.* **1991**, *44*, 8304–8307.
- (23) Lipp, M. J.; Jackson, D.; Cynn, H.; Aracne, C.; Evans, W. J.; McMahan, A. K. Thermal Signatures of the Kondo Volume Collapse in Cerium. *Phys. Rev. Lett.* **2008**, *101*, 165703.
- (24) Sternemann, C.; Volmer, M.; Soininen, J. A.; Nagasawa, H.; Paulus, M.; Enkisch, H.; Schmidt, G.; Tolan, M.; Schülke, W. Momentum-Transfer Dependence of X-Ray Raman Scattering at the Be K-Edge. *Phys. Rev. B: Condens. Matter Mater. Phys.* **2003**, *68*, No. 035111.
- (25) Soininen, J. A.; Ankudinov, A. L.; Rehr, J. J. Inelastic Scattering from Core Electrons: A Multiple Scattering Approach. *Phys. Rev. B: Condens. Matter Mater. Phys.* **2005**, *72*, No. 045136.
- (26) Bradley, J. A.; Moore, K. T.; van der Laan, G.; Bradley, J. P.; Gordon, R. A. Core and Shallow-Cored- to *f*-Shell Excitations in Rare-Earth Metals. *Phys. Rev. B: Condens. Matter Mater. Phys.* **2011**, *84*, 205105.
- (27) Haverkort, M. W.; Tanaka, A.; Tjeng, L. H.; Sawatzky, G. A. Nonresonant Inelastic X-Ray Scattering Involving Excitonic Excitations: the Examples of NiO and CoO. *Phys. Rev. Lett.* **2007**, *99*, 257401.
- (28) van der Laan, G.; Thole, B. T. Core Hole Polarization in Resonant Photoemission. *J. Phys.: Condens. Matter* **1995**, *7*, 9947–9988.
- (29) Fister, T. T.; Seidler, G. T. Multielement Spectrometer for Efficient Measurement of the Momentum Transfer Dependence of Inelastic X-Ray Scattering. *Rev. Sci. Instrum.* **2006**, *77*, No. 063901.
- (30) Gordon, R. A.; Seidler, G. T.; Fister, T. T.; Nagle, K. P. Studying Low-Energy Core-Valence Transitions with Bulk Sensitivity using q-Dependent NIXS. *J. Electron Spectrosc. Relat. Phenom.* **2011**, *184* (2011), 220–223.
- (31) Bradley, J. A.; Sen Gupta, S.; Seidler, G. T.; Moore, K. T.; Haverkort, M. W.; Sawatzky, G. A.; Conradson, S. D.; Clark, D. L.; Kozimor, S. A.; Boland, K. S. Probing Electronic Correlations in Actinide Materials using Multipolar Transitions. *Phys. Rev. B: Condens. Matter Mater. Phys.* **2010**, *81*, 193104.
- (32) Kotani, A.; Ogasawara, H. Theory of Core-Level Spectroscopy of Rare-Earth Oxides. *J. Electron Spectrosc. Relat. Phenom.* **1992**, *60*, 257–299.
- (33) Kotani, A.; Okada, M.; Jo, T.; Bianconi, A.; Marcelli, A.; Parlebas, J. C. Many Body Effect in Inner Shell Photoemission and Photoabsorption Spectra of La Compounds. *J. Phys. Soc. Jpn.* **1987**, *56*, 798–809.
- (34) Gordon, R. A.; Seidler, G. T.; Fister, T. T.; Haverkort, M. W.; Sawatzky, G. A.; Tanaka, A.; Sham, T. K. High Multipole Transitions in NIXS: Valence and Hybridization in 4*f* Systems. *Europhys. Lett.* **2008**, *81*, 26004.
- (35) Takegahara, K.; Aoki, Y.; Yanase, A. Slater-Koster Tables for *f* Electrons. *J. Phys. C: Solid State Phys.* **1980**, *13*, 583–588.
- (36) Harrison, W. A. Electronic Structure of *f*-Shell Metals. *Phys. Rev. B: Condens. Matter Mater. Phys.* **1983**, *28*, 550.
- (37) Ding, Y.; Chen, C. C.; Zeng, Q.; Kim, H. S.; Han, M. J.; Balasubramanian, M.; Gordon, R.; Li, F.; Bai, L.; Popov, D.; et al. Novel High-Pressure Monoclinic Metallic Phase of V<sub>2</sub>O<sub>3</sub>. *Phys. Rev. Lett.* **2014**, *112*, No. 056401.

(38) McMahan, A. K.; Held, K.; Scalettar, R. T. Thermodynamic and Spectral Properties of Compressed Ce Calculated Using a Combined Local-Density Approximation and Dynamical Mean-Field Theory. *Phys. Rev. B: Condens. Matter Mater. Phys.* **2003**, *67*, No. 075108.

(39) Dallera, C.; Gironi, M.; Palenzona, A.; Taguchi, M.; Annese, E.; Ghiringhelli, G.; Tagliaferri, A.; Brookes, N. B.; Neisius, Th; Braicovich, L.  $\alpha$ - $\gamma$  Transition in Metallic Ce Studied by Resonant X-Ray Spectroscopies. *Phys. Rev. B: Condens. Matter Mater. Phys.* **2004**, *70*, No. 085112.

(40) Casadei, M.; Ren, X.; Rinke, P.; Rubio, A.; Scheffler, M. Density-Functional Theory for *f*-Electron Systems: the Alpha-Gamma Phase Transition in Cerium. *Phys. Rev. Lett.* **2012**, *109*, 146402.

(41) Pickett, W. E.; Freeman, A. J.; Koelling, D. D. Local-Density-Functional Approach to the Isostructural  $\gamma$ - $\alpha$  Transition in Cerium Using the Self-Consistent Linearized-Augmented-Plane-Wave Method. *Phys. Rev. B: Condens. Matter Mater. Phys.* **1981**, *23*, 1266.

(42) McMahan, A. K. Combined Local-Density and Dynamical Mean Field Theory Calculations for the Compressed Lanthanides Ce, Pr, and Nd. *Phys. Rev. B: Condens. Matter Mater. Phys.* **2005**, *72*, 115125.

(43) Haule, K.; Oudovenko, V.; Savrasov, S. Y.; Kotliar, G. The  $\alpha$ - $\gamma$  Transition in Ce: A Theoretical View from Optical Spectroscopy. *Phys. Rev. Lett.* **2005**, *94*, No. 036401.

(44) Held, K.; McMahan, A. K.; Scalettar, R. T. Cerium Volume Collapse: Results from the Merger of Dynamical Mean-Field Theory and Local Density Approximation. *Phys. Rev. Lett.* **2001**, *87*, 276404.

(45) Mao, H. K.; Ding, Y.; Xiao, Y. M.; Chow, P.; Shu, J.; Lebegue, S.; Lazicki, A.; Ahuja, R. Electronic Dynamics and Plasmons of Sodium under Compression. *Proc. Natl. Acad. Sci. U. S. A.* **2011**, *108*, 20434–20437.

(46) Fister, T. T.; Vila, F. D.; Seidler, G. T.; Svec, L.; Linehan, J. C.; Cross, J. O. Local Electronic Structure of Dicarba-Closo-Dodecaboranes  $C_2B_{10}H_{12}$ . *J. Am. Chem. Soc.* **2008**, *130*, 925–932.

(47) Sugar, J. Potential-Barrier Effects in Photoabsorption. II. Interpretation of Photoabsorption Resonances in Lanthanide Metals at the *4d*-Electron Threshold. *Phys. Rev. B* **1972**, *5*, 1785.

(48) Mostofi, A. A.; Yates, J. R.; Lee, Y.-S.; Souza, I.; Vanderbilt, D.; Marzari, N. wannier90: A Tool for Obtaining Maximally-Localised Wannier Functions. *Comput. Phys. Commun.* **2008**, *178*, 685.

(49) Kresse, G.; Furthmüller, J. Efficiency of ab-Initio Total Energy Calculations for Metals and Semiconductors Using a Plane-Wave Basis Set. *Comput. Mater. Sci.* **1996**, *6*, 15–50.

(50) Kresse, G.; Furthmüller, J. Efficient Iterative Schemes for ab Initio Total-Energy Calculations Using a Plane-Wave. *Phys. Rev. B: Condens. Matter Mater. Phys.* **1996**, *54*, 11169–11186.

(51) Blöchl, P. E. Projector Augmented-Wave Method. *Phys. Rev. B: Condens. Matter Mater. Phys.* **1994**, *50*, 17953–17979.

(52) Kresse, G.; Joubert, D. From Ultrasoft Pseudopotentials to the Projector Augmented-Wave Method. *Phys. Rev. B: Condens. Matter Mater. Phys.* **1999**, *59*, 1758.

(53) Perdew, J. P.; Burke, K.; Ernzerhof, M. Generalized Gradient Approximation Made Simple. *Phys. Rev. Lett.* **1996**, *77*, 3865.

(54) Inokuti, M. Inelastic Collisions of Fast Charged Particles with Atoms and Molecules—the Bethe Theory Revisited. *Rev. Mod. Phys.* **1971**, *43*, 297–347.

(55) Bradley, J. A.; Sakko, A.; Seidler, G. T.; Rubio, A.; Hakala, M.; Hämäläinen, K.; Cooper, G.; Hitchcock, A. P.; Schlimmer, K.; Nagle, K. P. Reexamining the Lyman-Birge-Hopfield band of  $N_2$ . *Phys. Rev. A: At., Mol., Opt. Phys.* **2011**, *84*, No. 022510.